

Parameter Distribution Models for Estimation of Population Based Left Ventricular Deformation Using Sparse Fiducial Markers

Espen W. Remme*, Kevin F. Augenstein, Alistair A. Young, and Peter J. Hunter

Abstract—We present a method to estimate left ventricular (LV) motion based on three-dimensional (3-D) images that can be derived from any anatomical tomographic or 3-D modality, such as echocardiography, computed tomography, or magnetic resonance imaging. A finite element mesh of the LV was constructed to fit the geometry of the wall. The mesh was deformed by optimizing the nodal parameters to the motion of a sparse number of fiducial markers that were manually tracked in the images through the cardiac cycle. A parameter distribution model (PDM) of LV deformations was obtained from a database of MR tagging studies. This was used to filter the calculated deformation and incorporate *a priori* information on likely motions. The estimated deformation obtained from 13 normal untagged studies was compared with the deformation obtained from MR tagging. The end systolic (ES) circumferential and longitudinal strain values matched well with a mean difference of $0.1 \pm 3.2\%$ and $0.3 \pm 3.0\%$, respectively. The calculated apex-base twist angle at ES had a mean difference of $1.0 \pm 2.3^\circ$. We conclude that fiducial marker fitting in conjunction with a PDM provides accurate reconstruction of LV deformation in normal subjects.

Index Terms—Free-form deformation, host mesh deformation, left ventricular motion, parameter distribution models.

I. INTRODUCTION

A quantitative description of regional left ventricular (LV) wall deformation is essential for the diagnosis and evaluation of cardiac performance, and the evaluation of treatment. In order to quantify regional wall motion and deformation precisely, detailed information on the three-dimensional (3-D) motion of a large number of material landmarks is required. The LV deforms in a complex 3-D manner during systole, characterized by circumferential and longitudinal shortening, wall thickening, and torsion about the LV central axis [1]. The direction of maximum tissue contraction is usually obliquely aligned with

Manuscript received April 1, 2004; revised November 22, 2004. This work was supported in part by the Research Council of Norway under Grant 128267/320 and Grant 139327/300. The Associate Editor responsible for coordinating the review of this paper and recommending its publication was G.-Z. Yang. *Asterisk indicates corresponding author.*

*E. W. Remme was with the Bioengineering Institute, University of Auckland, New Zealand on leave from the Department of Circulation and Medical Imaging, Norwegian University of Science and Technology, Trondheim, Norway. He is now with the Institute for Surgical Research, Rikshospitalet University Hospital, 0027 Oslo, Norway (e-mail: espen.remme@medisin.uio.no).

K. F. Augenstein and P. J. Hunter are with the Bioengineering Institute, University of Auckland, Auckland, New Zealand (e-mail: k.augenstein@auckland.ac.nz; p.hunter@auckland.ac.nz).

A. A. Young is with the Department of Anatomy with Radiology, University of Auckland, Auckland, New Zealand (e-mail: a.young@auckland.ac.nz).

Digital Object Identifier 10.1109/TMI.2004.842458

respect to the major and minor axes of the LV, and in general are not aligned with any imaging plane. Currently, magnetic resonance (MR) tissue tagging is the most accurate and precise method for the noninvasive measurement of 3-D heart wall motion and regional strain. This method creates tags by presaturating planes of tissue, perpendicular to the imaging planes, with a short burst of radiofrequency pulses on detection of the R wave of the electrocardiography (ECG). The “tag-planes” appear on the image as a dark grid pattern that moves and deforms along with the myocardium. Analysis of this deformation then allows direct, noninvasive measurement of regional myocardial motion with high accuracy [1], [2]. Data from multiple slices (e.g., short- and long-axis views) can be merged into a coherent 3-D motion using a mathematical model in the form of a finite element (FE) mesh, which captures the shape and motion of the LV [2]. However, MRI is not as commonly available as other modalities such as echocardiography due to its relatively high cost, longer acquisition times, requirement for isolation from external radio frequency radiation, contraindications associated with MRI and increased difficulty of patient interventions.

A modality-independent method for calculating LV motion has been developed by [3]–[5] which is based on standard anatomical images that may be obtained from ultrasound, X-ray computed tomography (CT), and magnetic resonance imaging (MRI). The 3-D LV surfaces in successive frames are segmented and a shape-based tracking algorithm attempts to recover a point-to-point correspondence on successive surfaces by matching points with similar surface curvature. The estimated displacements are filtered by the use of a mathematical model with a constitutive law describing the mechanics of the heart wall that gives a probability for the displacement field. However, accurate modeling of heart mechanics requires a detailed knowledge of material architecture and hyper-elastic material law. A number of constitutive law models for cardiac tissue have been developed [6] based on biaxial [7]–[9] and shear [10] tests. A major difficulty with the application of these models is determining the spatial variation of parameters. Estimating constitutive law parameters from whole organ mechanics is a very ill-conditioned problem, partly because the incompressibility constraint means there is a high correlation between behavior along different axis.

In this study, we investigated the feasibility of a modality-independent approach to estimate LV motion, based on manual tracking of distinct anatomical landmarks (fiducial markers) on the LV in the anatomical images. The images can be derived from any anatomical tomographic or 3-D modality, such as

echocardiography, biplane cineangiography, CT, or MRI. In summary, the user places a small number of sparsely distributed fiducial markers on the images and tracks them over time. A FE fitting procedure is used to reconstruct the 3-D deformation of the LV based on the motions of the fiducial markers in the images. In the case of tomographic images, data from short- and long-axis slices are included in this optimization to reconstruct all components of the 3-D deformation. Since the solution is under-constrained, due to the sparse nature of the fiducial data set, *a priori* information on the probability distribution of possible LV motions is incorporated. The probability distribution of motion is derived from a historical database of MR tissue tagging cases, previously analyzed with FE modeling. A principal component analysis (PCA) of the displacements of the parameters of the FE models in the database is performed to produce a “parameter distribution model” (PDM). This is closely related to the “point distribution models” of [11] and [12] which were used to create statistical shape models. We modified this method to incorporate motion rather than shape [13], which was recently also done by [14]. The estimated motion fitted to the fiducial marker tracings was subsequently filtered through the PDM to provide realistic, robust solutions. An important feature of our method is that novel motions which lie outside the range spanned by the PDM are permissible, but are treated as unlikely.

Therefore, the first aim of this study was to develop a method for the estimation of LV wall deformation given the tracked displacements of fiducial markers in the images. In order to allow fiducial markers to be placed adjacent to the LV model and still have influence on the deformation, a host mesh deformation procedure (similar to free-form deformations) was developed. The second aim was to develop a filtering procedure to improve the calculated deformed geometry, incorporating information from the historical database via the PDM. To validate the method, fiducial marker fitting was performed on anatomical cine MR images in 13 normal volunteers. The estimated deformation was compared with the deformation obtained by 3-D reconstruction from MRI tagging data, in the same 13 normal volunteers.

II. METHODS

A. Imaging

Anatomical and tagged MR images were acquired in 13 normal volunteers (age 19–26, 4 female, 72 ± 16 kg, 174 ± 11 cm) who had no history of cardiac disease. These subjects were part of a control group for a previous study, details of which can be found in [15]. All imaging was performed on a 1.5 T Siemens Vision magnet with a phased array body coil. Prospectively gated untagged cardiac cine images were acquired in 8–9 short-axis slices and 3 long-axis slices using a segmented k-space pulse sequence ($TE/TR = 4.8/9.9$ ms, flip angle = 15° , FOV 280–350 mm, 7 or 9 views per segment, 128×256 image matrix) with view-sharing (giving 11–19 frames per slice). Each slice was acquired during a breath hold of 15–19 cardiac cycles at end-tidal lung volume. The short-axis slices spanned the heart from apex to base with a slice thickness of 8.0 mm and inter-slice gap of 2.0–4.5 mm. The long-axis image slices were acquired at equal 60° increments around

the LV central axis, starting at the plane passing through the mid-septum, center of the LV cavity and LV free-wall.

Short-axis tagged images of the heart were acquired at the same positions as the cine untagged images using a prospectively gated, view-shared, breath-hold, segmented k-space version of the SPAMM imaging sequence [15]. The tag spacing in the orthogonal grid pattern was 8 mm and the tag lines were oriented at 45° relative to the imaging axes. The imaging parameters were the same as those used for the breath-hold cine MRI acquisition described above, except for $TE/TR = 4.0/8.9$ ms. A set of six long-axis tagged image slices was also acquired at equal 30° increments around the LV central axis.

B. Finite Element Model Construction

For each case the LV endocardial and epicardial surfaces were manually segmented in the anatomical images for each time frame. A FE mesh was fitted to the segmented geometry by minimizing (in a least-squares sense) the distance between the segmented surface points and the surfaces of the FE mesh [16], [17]. A 16-element FE model was created in rectangular Cartesian coordinates consisting of 4 circumferential, 4 longitudinal, and 1 transmural elements. The geometric interpolation functions were cubic Hermite in the circumferential (ξ_1) and longitudinal (ξ_2) directions (for C^1 continuity) and linear in the transmural (ξ_3) direction. The interpolation is given by $u(\xi_1, \xi_2, \xi_3) = \sum_{k=1}^K \Psi_k(\xi_1, \xi_2, \xi_3) u_k$, where u represents the interpolated scalar function (e.g., x, y, or z coordinate) inside the element, Ψ_k are the tensor product element basis functions, and u_k represents the value of the scalar function or its derivatives at node k. The bicubic-linear interpolation results in 4 parameters per field per node of the model. These parameters directly define the value of the field (u), the first derivatives $\partial u / \partial \xi_1$ and $\partial u / \partial \xi_2$, and the cross derivative $\partial^2 u / (\partial \xi_1 \partial \xi_2)$ at each node.

C. Estimation of LV Deformation From MRI Tags

Tag stripes were located and tracked in the MR tagged images using a semi-automated tracking procedure, based on an active contour grid model, which has been previously described and validated [1], [2]. This enabled tag stripes to be tracked in each slice to determine the exact position and motion of several hundred points in the myocardium. Fig. 1 shows tracked tags from end diastole (ED) to end systole (ES) on a typical short-axis slice.

The 3-D motion best fitting the tracked image tag points was reconstructed with the aid of a FE model, as described previously [2]. Since the myocardium moves through the imaging plane from frame to frame, material points within the LV are generally imaged only once in the cine time sequence. Thus, the tracked image stripe points do not correspond to the same set of material points in the heart. However, initially (in frame 1 shortly after tag creation) the tags are straight and orthogonal to the image planes. Each stripe point in each subsequent frame, therefore, provides a one-dimensional (1-D) constraint on the displacement back to the initial frame: the displacement orthogonal to the original tag plane is known but the displacements parallel to the tag plane are not. In the present application, the

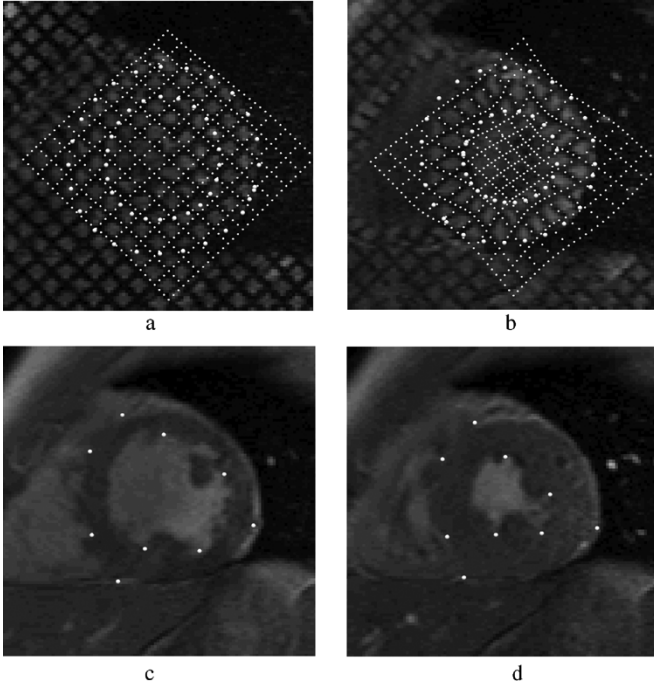


Fig. 1. Short-axis tagged MR images are shown at ED in (a) and ES in (b) with the tracked image stripe points. The larger circles outline the epicardial and endocardial surfaces. In (c) and (d), the anatomical (untagged) short-axis images at ED and ES are shown, respectively, with manually placed and tracked fiducial markers.

location of all the tracked stripe points for time t were determined within the FE model fitted to the segmented boundaries at time t as described above [this model is denoted $\mathbf{x}^t(\boldsymbol{\xi})$]. This allowed calculation of the material coordinates $\boldsymbol{\xi}_d^t$ of each tag point \mathbf{x}_d^t within the FE model at time t . The nodal parameters of the corresponding FE mesh at ED were then found by deforming $\mathbf{x}^t(\boldsymbol{\xi})$ so as to minimize

$$E(\mathbf{x}^t) = S(\mathbf{x}^t) + \sum_d \left[\mathbf{n}_d \cdot (\mathbf{x}^t(\boldsymbol{\xi}_d^t) - \mathbf{x}_d^{\text{ED}}) \right]^2 \quad (1)$$

The smoothing constraint $S(\mathbf{x}^t)$ is included to regularize the problem in case of nonuniformly distributed data. The tag points, \mathbf{x}_d^{ED} , are tracked tag points along the lines where the tag-planes intersect the images at ED. Each point has coordinates \mathbf{x}_d^{ED} and a normal vector \mathbf{n}_d (in practice the normal to the corresponding tag-plane at ED). Thus, only the component along the tag-plane normal is penalized in the error term (1). The reconstruction fits for every time $t > t_{\text{ED}}$ provide a series of geometries at ED.

Each of these ED geometries is associated with the segmented FE mesh at a subsequent time. For motion analysis it is more desirable to have a series of subsequent deformed models with one single reference state. This was achieved by deforming an FE mesh, fitted to the segmented surface points at ED ($\mathbf{x}^{\text{ED}}(\boldsymbol{\xi})$), to match the reconstructed displacement data generated from the reconstruction fits. The reconstructed displacement data was found as the position of the reconstructed tag point position at ED $\hat{\mathbf{x}}_d^{\text{ED}}$, corresponding to the position of the same material point at time t , \mathbf{x}_d^t . These allowed calculation of material coordinates $\boldsymbol{\xi}_d^{\text{ED}}$ within the ED model $\mathbf{x}^{\text{ED}}(\boldsymbol{\xi})$. This model is deformed

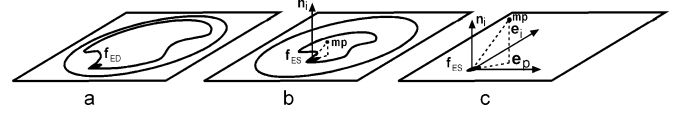


Fig. 2. Schematic short-axis image slice of the LV at ED shown in (a) with a fiducial marker (f_{ED}) placed at the intersection of the papillary muscle with the LV wall. The same imaging slice is shown in (b) at ES with the manually tracked fiducial marker (f_{ES}). The estimated deformation has caused the material point (mp) corresponding to the fiducial marker in (a) to move out of the imaging plane which is shown by its projection onto the plane along image-plane normal \mathbf{n}_i . Enlargement of the projection shown in (c). As the material point in general will move out of the imaging-plane the error component e_i along \mathbf{n}_i should be neglected, while only the error e_p in the imaging plane should be penalized when estimating the deformation.

to minimize (2) where there is no need for the tag plane normals as the through plane displacement has been reconstructed

$$E(\mathbf{x}^{\text{ED}}) = S(\mathbf{x}^{\text{ED}}) + \sum_d \left\| \left(\mathbf{x}^{\text{ED}}(\boldsymbol{\xi}_d^{\text{ED}}) - \mathbf{x}_d^t \right) \right\|^2 \quad (2)$$

D. Estimation of LV Deformation From Fiducial Markers

Fiducial markers, i.e., identifiable points or landmarks in the images that can be visually tracked from frame to frame, were manually identified and tracked in each cine anatomical (untagged) image. These points included the intersections of valves, papillary muscles and the right ventricular wall with the LV wall, and distinct trabecula structures on the endocardial surface. Fig. 1(c) and (d) shows tracked fiducial markers for images at the same location as Fig. 1(a) and (b).

The reconstruction of 3-D motion from fiducial markers is treated in a similar fashion to the tag reconstruction process. As for tag fitting, the model (material) coordinates of each fiducial marker are determined at ED within an ED model geometry. For tomographic imaging modalities, fiducial markers remain on the image plane which is fixed in space. The material point corresponding to the fiducial marker may, therefore, move out of the imaging plane, while the tracked image fiducial marker may be considered as a projection of the material point onto the image plane. This approximation assumes that the material point corresponding to the fiducial marker will have a projection along the image-plane normal onto the image plane onto the fiducial marker in the subsequent frame at time t , as in Fig. 2. In this case, instead of penalizing the error-component normal to the tag-plane, only the error in the imaging plane was penalized as shown in (3)

$$E(\mathbf{x}^{\text{ED}}) = S(\mathbf{x}^{\text{ED}}) + \sum_d \left\| \left(\mathbf{x}^{\text{ED}}(\boldsymbol{\xi}_d^{\text{ED}}) - \mathbf{x}_d^t \right) - \left(\mathbf{n}_d \cdot \left(\mathbf{x}^{\text{ED}}(\boldsymbol{\xi}_d^{\text{ED}}) - \mathbf{x}_d^t \right) \right) \mathbf{n}_d \right\|^2 \quad (3)$$

where \mathbf{n}_d is the image-plane normal for fiducial marker d , and \mathbf{x}_d^t and $\mathbf{x}^{\text{ED}}(\boldsymbol{\xi}_d^{\text{ED}})$ are the fiducial marker at time t and the corresponding model point inside the deforming ED mesh, respectively. Thus, only the tracked motion in the image plane is fitted, while not constraining through plane motion.

E. Host Mesh Deformation

Whereas tags were located inside the LV wall and, thus, inside the LV FE mesh, the fiducial markers were often obtained adjacent but outside the contiguous myocardial area modeled by the

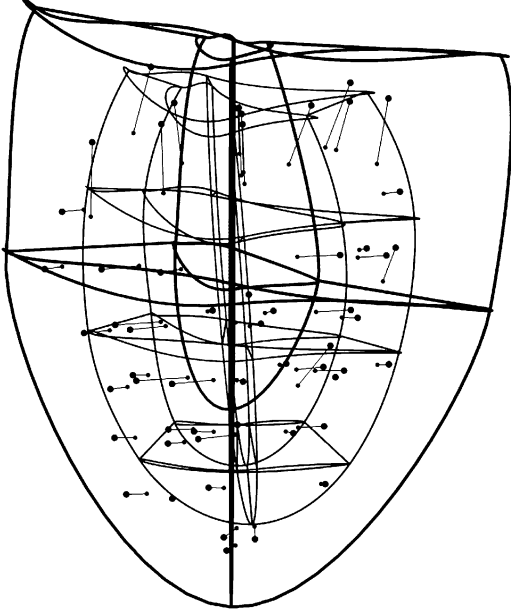


Fig. 3. The LV mesh (thin lines) embedded in the host mesh (thick lines) at ED. The fiducial markers at ED are shown with big circles projected onto their corresponding markers at ES (small circles).

LV FE model. This was because trackable fiducial markers usually occurred at the intersections of papillary muscles, trabeculae, mitral valve points, etc, with the LV myocardium. These could occur outside the domain of the LV model. In this case, the fiducial markers would not have appropriate model coordinates ξ_d^{ED} inside the ED LV mesh. This problem was solved by using a host mesh fitting procedure [17]. Briefly, we embedded the ED LV FE mesh and fiducial markers inside a larger host mesh, as seen in Fig. 3. The host mesh had 8 elements, 4 element circumferentially and 2 longitudinally with cubic Hermite interpolation in the circumferential and longitudinal directions and linear in the transmural direction and, thus, only half the number of mesh degrees of freedom of the 16-element LV model. The material coordinates within the host mesh of the LV model nodes and fiducial markers, ξ_n^H and ξ_d^H respectively, were calculated at ED. Note that each of these ξ^H -coordinates for a node or fiducial marker represent a material point inside the host mesh. The fiducial marker fitting procedure was applied on the host mesh, adjusting the host mesh nodal parameters to minimize (3) by least squares for each time t . After the host mesh was optimized, the new LV model nodal parameters, i.e., the value of $\mathbf{x}(\xi_n^H)$ together with the derivatives of \mathbf{x} with respect to the LV model coordinates ξ_1 and ξ_2 , were updated according to the new physical position of their material points inside the deformed host mesh. This produced the reconstructed LV FE model for time t , which was then passed to the filtering stage.

F. Construction of the PDM

We based our filtering algorithm on the point distribution models developed by [11], [12]. This technique used a database of points which are placed at corresponding places within the shape. A PCA of the covariance matrix allows the construction of a point distribution model, giving the statistical likelihood of any particular shape within the range of the model. In our case,

the fiducial markers may not be in the same positions from heart to heart, so a point distribution model cannot be formed from the fiducial markers themselves. Instead, we use the nodal parameters of the LV FE model from tagged data to construct a “parameter distribution model” (PDM). This is possible because the LV model nodes are placed in corresponding locations for each heart. The FE meshes fitted to the tag data were taken to be the “true” deformation, and were used for the PDM construction. The PDM describes the variation inherent in the database. The PDM was then used to filter the LV model resulting from fiducial marker fitting, in order to obtain a LV motion which is physiologically reasonable.

For each LV model in the database the nodal parameters were entered in a P element column vector, \mathbf{x}_s^t , for each time t as shown in (4)

$$\mathbf{x}_s^t = \left[x_1^t, \frac{\partial x_1^t}{\partial \xi_1}, \frac{\partial x_1^t}{\partial \xi_2}, \frac{\partial^2 x_1^t}{\partial \xi_1 \partial \xi_2}, y_1^t, \frac{\partial y_1^t}{\partial \xi_1}, \frac{\partial y_1^t}{\partial \xi_2}, \frac{\partial^2 y_1^t}{\partial \xi_1 \partial \xi_2}, z_1^t, \frac{\partial z_1^t}{\partial \xi_1}, \frac{\partial z_1^t}{\partial \xi_2}, \frac{\partial^2 z_1^t}{\partial \xi_1 \partial \xi_2}, \dots, \frac{\partial^2 z_K^t}{\partial \xi_1 \partial \xi_2} \right]^T \quad (4)$$

where s is the subject number, (x_1^t, y_1^t, z_1^t) are the coordinates at node 1 at time t , K is the number of nodes, ξ_1 is the circumferential and ξ_2 is the longitudinal coordinates of the elements of the FE mesh, and T is the transpose operator. Each subject’s parameter vector had length of $P = 480$, describing the 3-D shape of the LV model with $K = 40$ nodes. The difference vector $\mathbf{d}^\tau = (\mathbf{x}_s^\tau - \mathbf{x}_s^{\text{ED}})$ between the \mathbf{x}_s at time τ (in a normalized cardiac cycle time scale explained below) and ED described the deformation of each subject’s mesh. The mean \mathbf{d}_m^τ was calculated for all subjects and the matrix B^τ was formed by making each column, s , of B^τ equal to $\mathbf{d}_s^\tau - \mathbf{d}_m^\tau$. Using singular value decomposition (SVD) we found the orthonormal matrices U^τ and V^τ and the diagonal matrix S^τ such that $B^\tau = U^\tau S^\tau (V^\tau)^T$. The nullspace of B^τ was spanned by the matrix N^τ found by SVD of the transpose of B^τ : $(B^\tau)^T = Q^\tau \Sigma^\tau N^\tau$. Assuming the model parameters are distributed normally about the mean, the singular values are proportional to the standard deviation (SD) of the distribution in each orthogonal mode of variation given by the corresponding column of U^τ [18].

Due to differences in heart rate and length of the systolic and diastolic phases of the cardiac cycle, the frame times for each subject were converted to a normalized cardiac cycle time system. The length of the cardiac cycle (the time between two R-peaks of the ECG) was set to 1 s and the time for the ES frame was set to 0.35 s. The time increment for the frames between ED and ES was set to 0.35 s divided by the number of frames between ED and ES for the different subjects. A similar procedure was applied to calculate the times for the frames between ES and the next R-peak. We used a prospectively gated MR tag acquisition which meant the image acquisition would stop in advance of the second R-peak to “listen” for the ECG R-peak. This meant that there were no recordings in the last part of diastole. Thus, the PDM filter was only constructed for times up until $\tau = 0.6$ s in normalized cardiac cycle time.

For a new subject with deformation vector \mathbf{d}^τ , not included in the database used to calculate B^τ , the vector $(\mathbf{d}^\tau - \mathbf{d}_m^\tau)$ was projected onto the space spanned by the columns of U^τ , resulting in a vector, $\mathbf{p}^\tau = (U^\tau)^T (\mathbf{d}^\tau - \mathbf{d}_m^\tau)$, in which each element, p_i^τ , is

the projection length along its respective deformation mode or column \mathbf{U}_i^τ of \mathbf{U}^τ . The projection onto the nullspace of \mathbf{B}^τ was given by $\mathbf{p}_{N}^\tau = (\mathbf{N}^\tau)^T(\mathbf{d}^\tau - \mathbf{d}_m^\tau)$. The total deformation could then be expressed as $\mathbf{d}^\tau = \mathbf{d}_m^\tau + \mathbf{U}^\tau \mathbf{p}^\tau + \mathbf{N}^\tau \mathbf{p}_N^\tau$. In general, the columns of \mathbf{U}^τ will span out the space of deformations in a population (assuming the database training set is large enough). The inclusion of the nullspace will allow for a subject with novel deformations, i.e., motions not contained within the historical database. This is very important in clinical practice, since it is quite possible that the new case may represent a pathology not adequately characterized in the database of historical cases.

G. PDM Filtering

To filter a subject's calculated deformation, \mathbf{d}^τ , we could either exclude the modes with small singular values and/or apply weights to each mode. We used the weighting scheme to calculate the filtered deformation, \mathbf{d}_f^τ , as shown in (5), in which each mode in the span of \mathbf{U}^τ was weighted by w_i^τ and each mode in the nullspace of \mathbf{U}^τ was weighted by w_N^τ .

$$\mathbf{d}_f^\tau = \mathbf{d}_m^\tau + \sum_i w_i^\tau p_i^\tau \mathbf{U}_i^\tau + w_N^\tau \sum_j p_{N_j}^\tau \mathbf{N}_j^\tau \quad (5)$$

Since the singular values S_i^τ were proportional to the SDs of their respective modes \mathbf{U}_i^τ , $S_k^\tau > S_n^\tau$ implied a larger variation along mode \mathbf{U}_k^τ than \mathbf{U}_n^τ in the population. We, therefore, chose weights in (5) such that $w_i^\tau = S_i^\tau / \max_n(S_n^\tau)$, where $\max_n(S_n^\tau)$ was the maximum singular value. This biased the subject's deformation toward the mean deformation along modes that did not vary among the population whilst allowing individual variations along modes with a high degree of variability. The variation outside the range of the PDM (i.e., along each mode in the nullspace) was unknown and we had no reason to distinguish the weights for them. Since the most significant modes were found in \mathbf{U}^τ , we found it reasonable to weight the nullspace modes smaller than the smallest weight of the \mathbf{U}_i^τ terms: $w_N^\tau = c \cdot \min_n(S_n^\tau) / \max_n(S_n^\tau)$. We chose $c = 0.85$ for all our experiments. Once the filtered deformation \mathbf{d}_f^τ was calculated for the new subject, the final ED mesh coordinates was found as $\mathbf{x}^\tau = \mathbf{x}^{\text{ED}} + \mathbf{d}_f^\tau$.

H. Validation Experiments

In each of the 13 normal volunteers, the LV deformation obtained from the MR tags (tag modeling) was treated as the gold standard, and compared with the result of the filtered fiducial marker fitting process to obtain an error measure of goodness of fit. In order to construct an independent filter for each subject, tag models from the 12 other subjects were used in the construction of the PDM. The 12th singular value was zero, $S_{12}^\tau = 0$, due to the subtraction of the mean of every column in \mathbf{B}^τ . Thus, the first 11 orthonormal column vectors of \mathbf{U}^τ spanned out 11 modes in the "deviation from mean deformation"-space. The error was calculated as the mean Euclidean distance between the nodal positions obtained with the two methods

$$E^\tau = \frac{1}{K} \sum_{k=1}^K \sqrt{(x_{fk}^\tau - x_{tk}^\tau)^2 + (y_{fk}^\tau - y_{tk}^\tau)^2 + (z_{fk}^\tau - z_{tk}^\tau)^2} \quad (6)$$

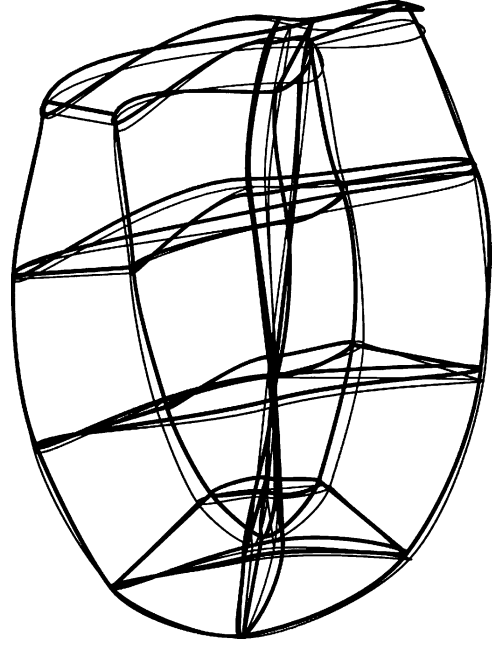


Fig. 4. Comparison of the ES meshes calculated by fitting tags (thick lines) and fiducial markers (thin lines). The average node error for this subject was 1.8 ± 0.8 mm between the two meshes.

where K is the number of nodes, x_{fk}^τ and x_{tk}^τ refer to the x-coordinates at node k for the estimated fiducial and tagged meshes, respectively.

In addition, ventricular wall strains and rotation about the central axis was compared between the two methods. Circumferential and longitudinal strains were calculated at 96 Gauss points in the mid-wall region of the upper 12 elements of the LV model. The radial strains and the apical region were not included, as there were typically insufficient tag planes to robustly characterize radial and apical strains. To calculate the basal rotation angle the center of gravity (CG) was found for the 4 endocardial base nodes at ED. The CG was subtracted from these node-coordinates and unit vectors were found from the origin toward each of the new node positions. The same was done for the mesh at ES and the dot product of the corresponding unit vectors at ED and ES represented the cosine of the rotation angle between ED and ES for a given node. These angles were also calculated for the 4 epicardial base nodes and all 8 angles were averaged to give the rotation angle of the base. The same procedure was applied to the 8 nodes closest to the apical nodes to find an estimate of the apical rotation. Ventricular twist was calculated as the difference between the apex and base rotations.

III. RESULTS

All results are given as mean value \pm SD. Typically, we were able to track 4–6 fiducial markers in each of the 3 long-axis images, and 4–9 in each of the short-axis images. The error between the nodes of the LV model at ES obtained by tag fitting and from filtered fiducial marker fitting ranged from 1.5 ± 0.6 mm to 2.3 ± 1.1 mm with an average of 1.8 ± 0.8 mm for the 13 subjects. Before filtering, the range was 3.6 ± 1.3 mm to 4.5 ± 2.3 and an average of 4.1 ± 1.8 mm. Fig. 4 shows an example of the ES meshes calculated with the two methods for a subject

TABLE I
MEAN DISTANCE BETWEEN NODES OBTAINED WITH TAGGED AND FIDUCIAL MARKER FITTING AFTER FILTERING FOR THE 13 SUBJECTS FOR THE DIFFERENT TIME FRAMES. THE NUMBER CORRESPONDING TO THE ES FRAME IS HIGHLIGHTED IN GREY FOR EACH SUBJECT. NUMBERS IN MILLIMETERS

Frame	Subject												
	1	2	3	4	5	6	7	8	9	10	11	12	13
2	1.3	1.2	0.9	0.9	1.2	0.6	1.7	0.6	0.9	0.7	0.7	0.7	0.9
3	1.8	1.1	1.4	1.6	1.5	1.0	1.6	1.0	1.5	1.0	1.4	0.9	0.8
4	2.0	1.2	1.7	2.2	1.7	1.0	1.8	1.3	1.8	1.2	1.5	1.3	0.9
5	2.1	1.5	2.0	2.5	1.8	1.1	2.2	1.3	2.0	1.5	1.7	1.5	1.3
6	2.5	1.6	2.2	2.4	1.8	1.5	2.1	1.4	2.0	1.7	2.1	1.6	1.7
7	2.2	1.5	2.3	2.3	1.8	1.4	1.8	1.4	1.8	1.7	2.1	1.8	1.8
8	2.2	1.6	2.0	2.3	1.7	1.4	2.0	1.6	1.9	2.0	2.0	1.9	1.9
9	1.7	2.1	2.0	2.3	1.8	1.5	2.5	2.1	2.0	1.7	1.9	2.2	1.9
10	1.6	2.9	2.2	2.7	2.2	1.6	3.7	3.5	2.0	1.6	1.9	4.4	1.8
11	2.3	5.0	2.7	5.6	4.8	2.0	6.7	5.5	3.6	2.1	2.0	3.6	2.0
12	2.9	2.3	4.2	4.5	6.5	3.0	2.0	2.5	4.1	4.6	2.0	1.8	4.0
13	4.6	2.6	5.6	2.6	3.8	5.0	2.2	2.2	1.6	4.8	3.7	1.9	5.1

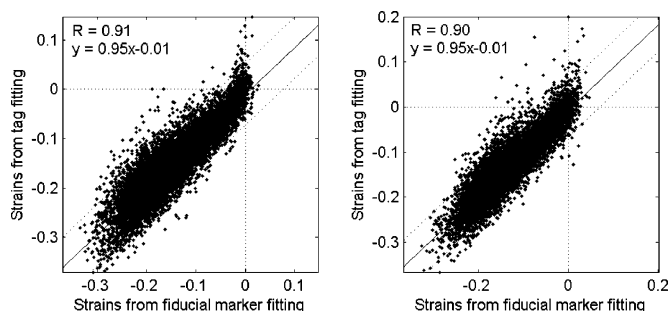


Fig. 5. Circumferential (left) and longitudinal (right) strains calculated from the deformation obtained by fitting tags and fiducial markers. Dotted lines are the ± 2 SD from the regression line (solid line).

with the average error of 1.8 ± 0.8 mm. The error after filtering for the various time frames for the different subjects is shown in Table I. The filter improved the error in all cases until the frames corresponding to the rapid filling phase. A marked increase of the error is seen in Table I for these frames.

For the 13 subjects the mean circumferential and longitudinal ES strains were $-20.3 \pm 5.0\%$ and $-17.7 \pm 4.8\%$, respectively, calculated with the ES meshes obtained from tag fitting. The same strains obtained by filtered fiducial marker fitting were $-20.2 \pm 3.9\%$ and $-18.0 \pm 3.3\%$. The average error for all 1248 (96 points times 13 patients) Gauss points between the ES strains calculated from the two methods was $0.1 \pm 3.2\%$ and $-0.3 \pm 3.0\%$ in the circumferential and longitudinal directions, respectively. Fig. 5 shows a regression plot between the strains obtained with the two fitting procedures for all frames from ED until the rapid filling phase. The correlations were $R = 0.91$ and $R = 0.90$ for the circumferential and longitudinal strains, respectively.

The mean basal rotation angle at ES for the 13 subjects was $-6.5 \pm 2.5^\circ$ and $-5.7 \pm 1.2^\circ$ calculated with tag modeling and filtered fiducial marker fitting, respectively, with a mean error of $0.8 \pm 2.1^\circ$ between the two methods. The mean apical rotation angle at ES was $11.6 \pm 3.6^\circ$ and $12.7 \pm 2.4^\circ$, respectively, with a mean error of $1.0 \pm 2.3^\circ$ between the two methods.

IV. DISCUSSION

In this paper, we have presented a new method for estimating LV wall motion using fiducial markers. *A priori* knowledge of

the probability distribution of feasible deformations was incorporated via the PDM to improve the solution, which is ill posed due to the sparsity of the data. The PDM was constructed from MR tagging studies, which is the current gold standard for non-invasive deformation estimation. The reconstruction method can be applied to a variety of imaging modalities, including conventional MRI, echocardiography, and computed tomography (CT). In all these cases, fiducial markers can be identified at the intersections of valves, papillary muscles and trabeculae with the LV myocardium. Note that the location of the imaging planes do not need to coincide with the imaging planes used in the construction of the PDM, since the parameter distributions are defined from a FE model of the 3-D geometry. Although fiducial markers were tracked manually in this study, automated techniques may be utilized such as shape-based tracking procedures [3]. However, they should make use of the rough structure of trabeculae and papillary muscles (and epicardial structures such as coronary arteries) in order to accurately reproduce myocardial motion, since gross curvature changes commonly occur during the cardiac cycle. In the case of echocardiography, tissue Doppler information may provide some help to trace points in the images through the cycle [19], or perhaps speckle tracking [20], [21] could replace the manual fiducial marker tracking. Any other 3-D imaging modality that provides fiducial markers may also be used, including biplane coronary angiography, in which the bifurcations of the coronary arteries can be tracked in 3-D and used as material landmarks [22].

For data from tomographic imaging modalities, it is necessary to obtain images from two orthogonal perspectives, i.e., short- and long-axis, to calculate any through plane motion of the myocardium. One source of error is that the tracked fiducial markers are assumed to be the projections of the corresponding material points onto the image plane. Unlike MR tags, which are created orthogonal to the imaging plane, there may be some component of the fiducial marker motions parallel to the imaging plane which is not imaged due to through plane motion. If the imaging orientations are oriented in the short- and long-axis planes, this error can be minimized by only tracking those anatomical landmarks which belong to structures approximately orthogonal to the imaging plane. In the case of centrally located long-axis images, the mitral and aortic valves intersect with the image plane approximately at right angles. Similarly,

the papillary muscles and endocardial trabeculae are approximately longitudinally oriented and, thus, are orthogonal to the short-axis images. The through plane component of the motion is largest at the base, which may descend 10–15 mm toward the apex during systole [23]. Therefore, the error due to fiducial marker projection may be expected to be largest at the base. However, we found that the basal rotation was very similar between the tagging and fiducial marker reconstructions, indicating that the effect of this approximation is small.

The accuracy of the fiducial marker tracing depends largely on image quality. Also some landmarks may be easier to identify and track than others. The fitted motion will be influenced by variations in the fiducial marker tracking. However, the PDM filtering step will remove or decrease the motion if it lies outside the allowed variation of the PDM filter. Generally, the more tracked fiducial markers the better the fit to any regional motion. The fiducial markers are used to fit the deformation of the host mesh. The fit of the host mesh depends not only on the number of fiducial markers but also the distribution of these inside the mesh. In the worst case scenario where there are only a few fiducial markers inside a region of the mesh, removal of or changes to these fiducial markers will significantly alter the fitted motion, whereas if some fiducial markers are removed or changed in a region where there are plenty of other fiducial markers the result will be less affected.

The method was applied to 13 cases of untagged MR tomographic cine imaging. The resulting deformation was similar to that obtained from MR tagging for all time frames until the rapid filling phase. For these frames the Euclidean distance between nodal positions estimated with the two methods was small, as were differences between circumferential and longitudinal Lagrangian strains and the calculated rotation angles. The marked increase of the Euclidean distance that was seen for the frames after the ES frame approximately corresponded to the rapid filling phase. During this phase there are large deformations occurring in just a short time period and there may be larger individual variations which may have caused the filter to perform badly during this phase. The error seemed to be reduced again for some subjects a few frames later which may indicate that the filter will perform better again at the last phase of the cardiac cycle. Tagged MR measurements over the whole cycle are necessary to construct the filter for the last phase of the cycle too. We used prospectively gated MR tagged measurements which excluded the last part of the cycle, but with new retrospectively tagged MR measurements, this could now be done.

The developed filter is based on a database representing the “true” distributions of deformations obtained from MR tagging measurements. The deformation from several subjects was entered in matrix form and a singular value decomposition was used to extract the most significant modes of deformations as the columns in the matrix U , each with a corresponding SD proportional to the singular value. For each of the 13 subjects, we used the other 12 to obtain a filter independent of the current subject. This gave 11 deformation modes plus a mean deformation. The subject’s deformation was projected onto this space, and the filtered deformation was a sum of the projected deformation modes weighted with the mode’s SD. This technique is similar to the filtering procedure described by [11] and [12],

in which the contribution of each mode is scaled according to a factor (D_{\max}/D) , where $D_{\max} \leq D$ is chosen by the user and $D = \sum_i (p_i/S_i)^2$. In contrast to [11], [12], and [14], we also allowed deformations from the nullspace of the training set of normal subjects, in order to enable deformations outside the range of the PDM. In the clinical domain, it is essential that new pathologies which may not be well characterized in the historical database can be modeled. However, the method was only validated on normal subjects in this study. Its applicability to patients with abnormal heart motion needs to be investigated further. The filter applied in this paper is developed from a population of normal subjects and has not been tested on patients with abnormal deformations. However, the technique can obviously be applied using populations of patients with disease.

Note that the filter can be viewed as a method of interpolating information supplied by the tracked fiducial markers. If the population describes a narrow range of shape and motion variations, and a particular individual is well described by these variations, then relatively few fiducial markers are needed. The nullspace is included in the filter to account for subjects with deformations that lie outside the span of the population. If fiducial marker data imply deformations outside the span of the population, then these can be accommodated. This makes the filter population based, but not population specific. Although matching the population to the individual (such as would be possible if the patient disease was known *a priori*) is desirable in that fewer fiducial markers are required, it is likely that a population containing a wider range of strain/shape variances can be applied and still only require a relatively small number of fiducial markers. That is because the deformations described in the population are still likely to be only a small subset of deformations obtainable from the unfiltered mathematical model.

The tuning of the filter is dependent on the number of subjects. In the present validation study, the number of subjects included in the PDM was very small, leading to only 11 modes in the PDM. Thus, adding a new subject to the training set will result in one more mode in U . As more and more subjects are included, the singular values and modes will converge and eventually new models will not add information to the PDM. This would allow only the most significant modes (those with singular values above a defined threshold) to be included in the PDM. Given a large database of subjects, the most significant modes would be included in U and individually weighted in the filter. The modes below the threshold would be included in the nullspace and filtered with equal weight. In the future, other constraints may be added to the PDM filter, including the isovolumetric property of myocardial tissue.

The PDM requires a standard FE mesh structure and orientation, with each parameter in the model governing the shape at a specific location within the LV which corresponds between cases. This was done by aligning the LV long-axis with the x-axis of the model, and the model y-axis with the middle of the right ventricle. Nodes were then placed in standard locations. Although the nodal parameters are in approximately the same locations with respect to the heart anatomy, they do not correspond to uniquely identifiable landmarks as are commonly used in PCAs. Thus, the PCA of shape and motion variation may in-

clude errors due to the lack of homologous points that can be identified from heart to heart.

In general, the LV FE mesh should contain sufficient degrees of freedom (mesh resolution) to reconstruct the gold standard data (in our case MR tags) to a desired level of accuracy (in our case less than one pixel). Given higher resolution data, a higher resolution model could be employed which captures the motion accurately. The PDM would then be modified to incorporate the increased model complexity and, thus, be able to handle population variations in the finer resolution of the motion. As a rule of thumb, the number of free parameters of the FE mesh should roughly match the number of constraints from the data. The tagging procedure gives roughly 3000 tag points in the LV wall, each of which provides a 1-D constraint to the fitting, which, thus, effectively gives roughly 1000 points. Our mesh has 480 parameters and is, thus, well matched to the acquired data.

The presented fiducial marker fitting procedure has the potential of working in a real time interactive post-processing environment, similar to the guide point modeling method developed for the fast estimation of LV mass and volumes [24]. In this implementation, an initial FE model was deformed in real time to every newly placed guide-point, minimizing the distance between the points and the model surfaces. In the present feasibility study, interaction was not investigated, however it would be straightforward to develop an interactive deformation estimation system in which an initial geometry could be obtained by geometric guide point modeling, and deformed using fiducial marker fitting. The calculation should be possible to perform in real time as there are relatively few mesh parameters and data points, the optimizations are performed with least squares and the filtering step is very fast. Seeing the resulting deformed mesh superimposed on the images will also have the advantage of being able to manually correct the fiducial marker positions to obtain a better fit to the actual geometry.

ACKNOWLEDGMENT

The authors would like to thank Dr. T. Gentles, Dr. B. Cowan and Dr. C. Occleshaw for the MR datasets used in this study.

REFERENCES

- [1] A. A. Young, C. M. Kramer, V. A. Ferrari, L. Axel, and N. Reichek, "Three-dimensional left ventricular deformation in hypertrophic cardiomyopathy," *Circulation*, vol. 90, pp. 854–867, Aug. 1994.
- [2] A. A. Young, D. L. Kraitchman, L. Dougherty, and L. Axel, "Tracking and finite element analysis of stripe deformation in magnetic resonance tagging," *IEEE Trans. Med. Imag.*, vol. 14, no. 3, pp. 413–421, Sep. 1995.
- [3] P. Shi, A. J. Sinusas, R. T. Constable, E. Ritman, and J. S. Duncan, "Point-tracked quantitative analysis of left ventricular surface motion from 3-D image sequences," *IEEE Trans. Med. Imag.*, vol. 19, no. 1, pp. 36–50, Jan. 2000.
- [4] X. Papademetris, A. J. Sinusas, D. P. Dione, and J. S. Duncan, "Estimation of 3D left ventricular deformation from echocardiography," *Med. Image Anal.*, vol. 5, pp. 17–28, Mar. 2001.
- [5] X. Papademetris, A. J. Sinusas, D. P. Dione, R. T. Constable, and J. S. Duncan, "Estimation of 3-D left ventricular deformation from medical images using biomechanical models," *IEEE Trans. Med. Imag.*, vol. 21, no. 7, pp. 786–800, Jul. 2002.
- [6] J. D. Humphrey, *Cardiovascular Solid Mechanics: Cells, Tissues, and Organs*. New York: Springer-Verlag, 2001.
- [7] D. T. K. Malcolm, P. M. F. Nielsen, P. J. Hunter, and P. G. Charette, "Strain measurement in biaxially loaded inhomogeneous, anisotropic elastic membranes," *Biomechan. Model. Mechanobiol.*, vol. 1, pp. 197–210, 2002.
- [8] D. M. Flynn, G. D. Peura, P. Grigg, and A. H. Hoffman, "A finite element based method to determine the properties of planar soft tissue," *J. Biomech. Eng.*, vol. 120, pp. 202–210, Apr. 1998.
- [9] P. G. Charette, P. J. Hunter, and I. W. Hunter, "Large deformation mechanical testing of biological membranes using speckle interferometry in transmission. II: Finite element modeling," *Appl. Opt.*, vol. 36, pp. 2246–2251, Apr. 1997.
- [10] S. Dokos, B. H. Smail, A. A. Young, and I. J. LeGrice, "Shear properties of passive ventricular myocardium," *Am. J. Physiol.*, vol. 283, pp. H2650–H2659, Dec. 2002.
- [11] T. F. Cootes, C. J. Taylor, D. H. Cooper, and J. Graham, "Active shape models—their training and application," *Comp. Vis. Image Understanding*, vol. 61, pp. 38–59, Jan. 1995.
- [12] T. F. Cootes, A. Hill, C. J. Taylor, and J. Haslam, "The use of active shape models for locating structures in medical images," *Image Vis. Comput.*, vol. 12, pp. 355–366, Jul. 1994.
- [13] E. W. Remme, A. A. Young, K. F. Augenstein, and P. J. Hunter, "Estimation of left ventricular deformation using fiducial markers," in *Proc. World Congr. Medical Physics and Biomedical Engineering*, Sydney, Australia, 2003, Paper no. 3932.
- [14] R. Chandrashekar, A. Rao, G. I. Sanchez-Ortiz, R. H. Mohiaddin, and D. Rueckert, "Construction of a statistical model for cardiac motion analysis using nonrigid image registration," in *Proc. IPMI*, 2003, pp. 599–610.
- [15] A. A. Young, B. R. Cowan, C. J. Occleshaw, H. C. Oxenham, and T. L. Gentles, "Temporal evolution of left ventricular strain late after repair of coarctation of the aorta using 3D MR tissue tagging," *J. Cardiovasc. Magn. Reson.*, vol. 4, pp. 233–243, May 2002.
- [16] C. Bradley and A. Pullan, "Geometric modeling of the human torso using cubic Hermite elements," *Ann. Biomed. Eng.*, vol. 25, pp. 96–111, 1997.
- [17] J. W. Fernandez, P. Mithraratne, S. Thrupp, M. H. Tawhai, and P. J. Hunter, "Anatomically based geometric modeling of the musculo-skeletal system and other organs," *Biomech. Model. Mechanobiol.*, vol. 2, pp. 139–155, Mar. 2004.
- [18] R. A. Johnson and D. W. Wichern, *Applied Multivariate Statistical Analysis*. Upper Saddle River, N.J.: Prentice-Hall, 1982, pp. 362–363.
- [19] S. I. Rabben, A. H. Torp, A. Stoylen, S. Sjordahl, K. Bjornstad, B. O. Haugen, and B. Angelsen, "Semiautomatic contour detection in ultrasound M-mode images," *Ultrasound Med. Biol.*, vol. 26, pp. 287–297, Feb. 2000.
- [20] K. Kaluzynski, X. Chen, S. Y. Emelianov, A. R. Skovoroda, and M. O'Donnell, "Strain rate imaging using two-dimensional speckle tracking," *IEEE Trans. Ultrason. Ferroelectr. Freq. Control.*, vol. 48, no. 4, pp. 1111–1123, Jul. 2001.
- [21] T. Anderson and W. N. McDicken, "Measurement of tissue motion," in *Proc. Inst. Mech. Eng.*, vol. 213, 1999, pp. 181–191.
- [22] A. A. Young, P. J. Hunter, and B. H. Smail, "Estimation of epicardial strain using the motions of coronary bifurcations in biplane cineangiography," *IEEE Trans. Biomed. Eng.*, vol. 39, no. 5, pp. 526–531, May 1992.
- [23] W. J. Rogers Jr, E. P. Shapiro, J. L. Weiss, M. B. Buchalter, F. E. Rademakers, M. L. Weisfeldt, and E. A. Zerhouni, "Quantification of and correction for left ventricular systolic long-axis shortening by magnetic resonance tissue tagging and slice isolation," *Circulation*, vol. 84, pp. 721–731, Aug. 1991.
- [24] A. A. Young, B. R. Cowan, S. F. Thrupp, W. J. Hedley, and L. J. Dell'Italia, "Left ventricular mass and volume: fast calculation with guide-point modeling on MR images," *Radiology*, vol. 216, pp. 597–602, Aug. 2000.